Chopped PHT-S spectra of faint sources

R. J. Laureijs
ISO Data Centre, Astrophysics Division, ESA, Villafranca, Spain

Version 2
26 September 2000

Abstract

To provide a better judgement whether features in a PHT-S spectrum are real, very deep and repeated tri-angular chopped observations of an "empty sky" were analyzed. It is found that the noise characteristics of the PHT-S subsystem in chopped mode are well-behaved for a large fraction of the channels in the array. The noise per measurement as determined by PIA is a good measure of the measurement-to-measurement scatter and scales with $t_{meas}^{-0.5}$. The channel to channel noise is uncorrelated. However, the channels with high noise characteristics exhibit a higher noise (by 40%) than expected from a $\sqrt{t}$ dependency. Tables with NEFDs are presented which can be used to give an independent prediction of the noise per channel.

1 Introduction

Deciding whether a faint source feature in a PHT-S spectrum is real or not depends on a number of assumptions about the estimated measurement noise. The validity of these assumptions in case of deep PHT-S chopped observations is investigated in this report. In particular, the following issues are checked for validity:

- does the statistical noise per channel as derived by PIA (or OLP) represents the uncertainty of the flux in a PHT-S channel?
- how does the noise scale with integration time?
- is the channel to channel noise similar to the statistical noise per channel, and
- is the flux/noise in a PHT-S spectrum independent from channel to channel?

For this investigation, very deep (4096 s) triangular-chopped PHT-S observations have been selected on a source which was not detected due to wrong coordinates. The observations were repeated 6 times on three different revolutions, using identical instrumental settings. These measurements provide an excellent database for checking the instrument stability, repeatability, and the noise properties of the detectors. In addition, since no source is detected, the observations can be used to accurately determine the PHT-S detection limits for both chopped and staring observations (see also below).

2 Observational data

In Table 1 a summary of the observational parameters is given. The coordinates of the target LHS 474 as entered by the observer are incorrect. The real source coordinates as listed by SIMBAD are RA: 19 16 58.10, Dec: +05 09 11.1 (J2000), which is more than one arcminute away from the pointing position. This explains the non-detection. The observations on the same (wrong) position were repeated 6 times, two consecutive pairs were observed over 3 revolutions (revs 134, 139, and 145).

Table 1: *Observing parameters.*

Target:	LHS 474/VB 10 (mispointing)
Obs/Props ID:	CTINNEY, CTINNEY1
Source Coordinates:	RA 19 17 0.3, Dec 05 10 23.5;
	l =40.4605, b =–3.2997
AOT:	PHT40, repeated 6 times
TDT:	134014, 134015, 139002, 139003, 145020, 145021
Wavelength:	2×64 channels,
	2.47–4.87 μm (SS), 5.84–11.62 μm (SL)
Aperture:	$24'' \times 24''$
observing mode:	triangular chopped
chop throw:	$45''$
measurement time:	4096 s
plateau time:	128 s
reset interval time:	32 s

3 Data Processing with PIA 9.0.1

3.1 Source Processing

We have processed the data using PIA version 9.0.1. The main processing steps for chopped PHT-S observations were applied with the following non-standard adjustments:

- ramp subdivision to 4 s per subramp
- signal deglitching: local box of 12 signals, and 2.5 σ threshold for signal rejection.
- no discard of the first 50% of the signals on a chopper plateau
- no drift recognition on a chopper plateau.

Before we decided on this approach, several sub-ramp times have been considered. It turns out that the 4 s sub ramps gave the narrowest distribution of the flux uncertainties computed by PIA. In addition, the PIA option weighted/not-weighted means was tested. It is found the that the weighted mean gave less strong outliers in the noise distribution than no error weighting. Therefore, the default option (weighting) was adopted. The photometric calibration was performed using the calibration developed for chopped PHT-S observations (Acosta-Pulido, 1999a).

The processing has been repeated by taking only the first half and first quarter of the (SRD level) signals in order to mimic 2048 s and 1024 s observations.

3.2 Sky background processing

The sky background for each observation has been determined by processing the SRD buffer as if it concerned a staring observation. This can be done by changing the following parameters in the phtsrd structure:
"chop" is set to 0.0
"step" is set to 1

The modified SRD buffer is then processed using the OLP9 dynamic calibration method after signal deglitching (as in previous section) and default dark signal subtraction. For a description of the dynamic PHT-S calibration we refer to Acosta (1999b).

4 Results and Analysis

4.1 Analysis of the statistical noise per channel

The resulting background subtracted source spectra are presented in Figure 1. Note that, since we have plotted Jy versus wavelength, the noise in Jy should increase with increasing wavelength for a constant noise power (in W) per pixel.

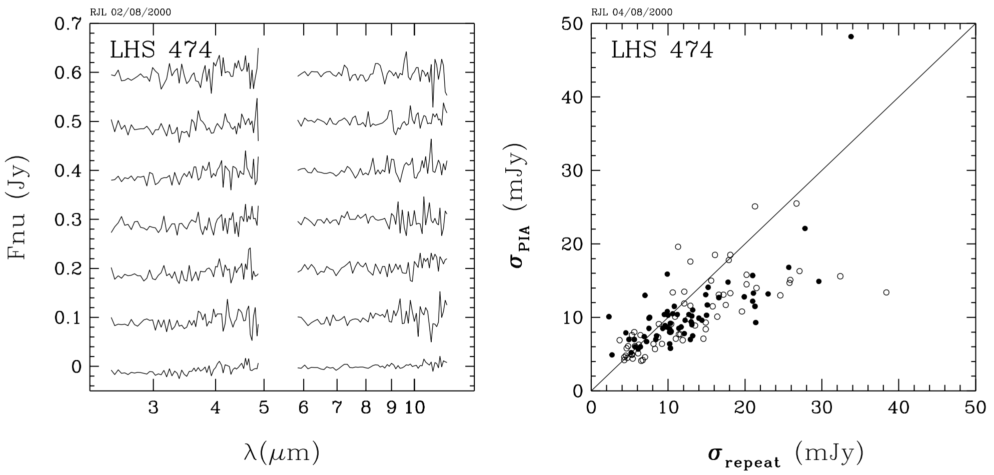

Figure 1: **Left panel:** *Composite of the individual PHT-S observations. The lowest spectrum is the average of the other 6. Except for the average spectrum, different constants are added to the individual spectra for better comparison.* **Right panel:** *The average rms per channel from PIA as a function of the rms derived from the 6 observations. Open symbols refer to PHT-SL channels, filled symbols to PHT-SS; the line is the identity.*

In Figure 1 we included the correlation between the average uncertainty per channel as derived from the individual uncertainties obtained by PIA (σ_{PIA}) and the rms per channel from the 6 measurements (σ_{repeat}). If the signal-to-signal scatter in a measurement would be the only source of uncertainty, and if the uncertainties from PIA are correctly measuring the rms of this scatter then:

$$\sigma_{PIA} = \sqrt{\frac{\sum \sigma_i^2}{N}} \quad \text{and} \quad \sigma_{repeat} \tag{1}$$

must be the same. In Eqn. 1 is σ_i the PIA uncertainty for measurement i and N (=6) the total number of measurements. The right panel in Figure 1 shows clearly that σ_{PIA} is comparable to σ_{repeat} for σ_{repeat} less than 10 mJy, for higher values of σ_{repeat}, σ_{PIA} underestimates the measurement to measurement scatter.

4.2 Time dependence of the noise, NEFD

We have repeated the processing for only the first half and the first quarter of the observations thereby mimicking observations with 2048 s and 1024 s measurement times. The observations have been processed in exactly the same way as for the 4096 measurements and σ_{repeat} was determined for this integration time. The resulting correlations between σ_{repeat} for 2048 and 4096 s, and between 1024 and 4096 s integration times are presented in Figure 2.

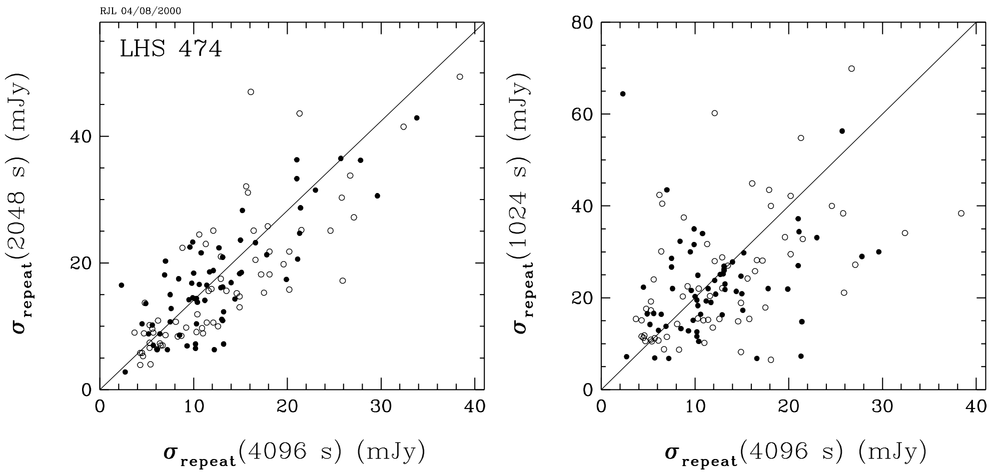

Figure 2: **Left panel:** *The rms derived from the 6 observations of 2048 s plotted as a function of the same noise for 4096 s integration time. Open symbols refer to PHT-SL channels, filled symbols to PHT-SS; the line indicates* $\sigma_{repeat}(2048\,s) = \sqrt{2}\times\sigma_{repeat}(4096\,s)$. **Right panel:** *same figure but the noise of 1024 s integration time versus 4096 s; the solid line is* $\sigma_{repeat}(1024\,s) = 2\times\sigma_{repeat}(4096\,s)$

Figure 2 shows that for the "good" channels with low noise characteristics the rms scales with $\sqrt{t}$. However, for a large fraction of the high noise channels the noise in the longer integration is slightly higher than expected from a $\sqrt{t}$ law.

Regression analysis - force fitting though the origin - shows that the mean ratio in the 2024 and 4096 s noise correlation is 1.28±0.08 which is close to the expected $\sqrt{2}$=1.41. The same analysis for $\sigma_{repeat}(4096\,s)$ > 20 mJy yields 1.34±0.13, closer to $\sqrt{2}$ but still slightly lower. The correlation between the noise of 1024 s versus 4096 s gives a slope of 1.61±0.17 which is also lower than the expected value of 2. The observed correlations are shallower than expected because the most noisy channels do not follow the $\sqrt{t}$ decrease.

The results show that the noise for most of the PHT-S channels in chopped spectra scales with time in the conventional way via $\sqrt{t}$.

Our values of $\sigma_{repeat}(4096\,s)$ and σ_{PIA} can be used to estimate the NEFDs per channel for deep chopped observations with $t_{meas} > 512\,$s:

$$\Delta F_\nu = \max(\sigma_{repeat}, \sqrt{\frac{\sigma^2_{repeat} + \sigma^2_{PIA}}{2}}). \tag{2}$$

Eqn. 2 has been considered to favour σ_{repeat} for those channels where the noise by PIA is underestimated. The resulting values of ΔF_ν are listed in Tables 4 and 5, see also Figure 3.

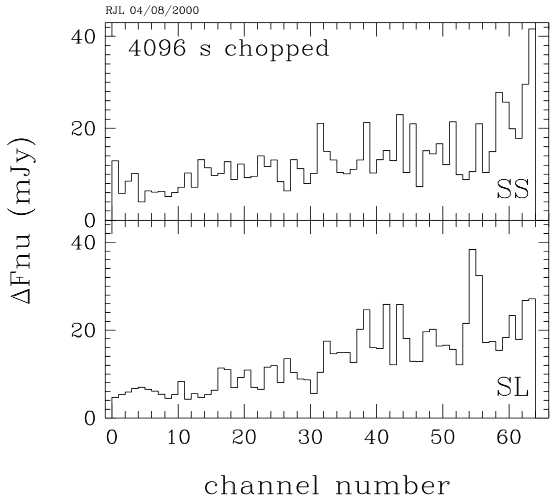

Figure 3: *The noise per channel for a 4096 s chopped observation. These values can be used to determine the noise of a given channel in case of a deep chopped measurement (t_{meas} > 512 s), the noise follows from $\sigma = \Delta F_\nu \sqrt{4096/t_{meas}}$*

4.3 Channel to channel noise in a spectrum

In principle, in case of a flat spectrum and an accurate spectral response function, it is expected that average noise over a number of channels should be the same as the cartesian average of the noise estimates of the individual channels. In the previous sections we have shown that the PIA noise estimate for a given "good" channel is a measure for the noise in that channel. Can these uncertainties be used to assess noise in e.g. the continuum of a PHT-S spectrum?

The average spectrum (on source t=3.4 hours, see Figure 1) was smoothed with a function which averages two pixels:

$$s_{new}(i) = s(i-1)/4 + s(i)/2 + s(i+1)/4 \tag{3}$$

The smoothed spectrum was subtracted from the individual spectra. Each of the 6 remaining residual noise spectra have been subdivided in groups of 16 consecutive channels from which we derived the dispersion.

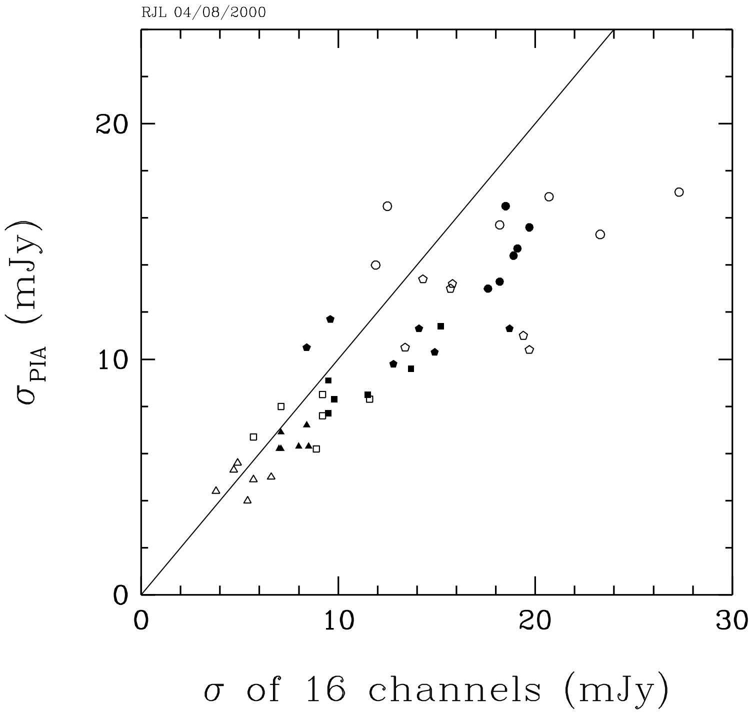

Figure 4: *The mean dispersion over 16 consecutive channels estimated from the PIA noise per channel (σ_{PIA}) plotted as a function of the actual dispersion of the residual fluxes of these channels. Each symbol represents 16 consecutive channels in each of the 6 spectra. Different symbols indicate different intervals of channels - triangles: channels 1–16, squares: 17–32, pentagons: 33–48, and circles: 49–64. Filled symbols refer to PHT-SS, open symbols to PHT-SL.*

In Figure 4 shows that the first 32 channels of each PHT-S array have the same scatter as can be predicted (by PIA) from the signal distribution on a measurement. However, for the long wavelength part of each PHT-S array the channel-to-channel noise is systematically higher than what is estimated by PIA. In particular, for channels 49–64 of PHT-SL the channel-to-channel dispersion ranges from 12–28 mJy, whereas the σ_{PIA} predicts a significantly smaller range of 14–18 mJy. The trend in Figure 4 is identical to what is found in Figure 1, suggesting a similar cause namely that the noise per channel by PIA is underestimated for the high noise channels. The underestimation is about 40% but can be as high as 80%, for channels 33–64 of both arrays.

If the underestimation by PIA is the only cause of the trend in Figure 4 then it is concluded that the channel-to-channel noise is identical to what can be expected from the noise per channel as determined from the repetition of identical observations, see Figure 3.

4.4 Chopper offsets for PHT-S?

The mean on–off PHT-S spectrum is presented in Figure 5. The spectrum is clearly not flat but shows that most of the baseline of PHT-SS and the first half of PHT-SL is significantly below zero and that the SS and SL spectral rise towards longer wavelengths.

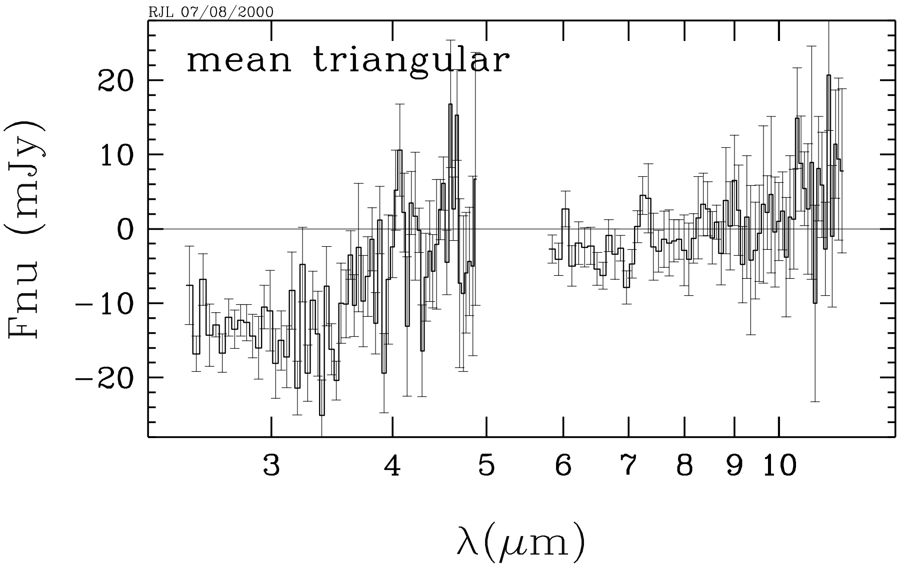

Figure 5: *The mean PHT-S spectrum of the 6 observations discussed in this report, the total on source integration time is* $6{\times}2048s$ = *3.41 hours. The error bars are the uncertainty of the mean* $\sigma_{repeat}/\sqrt{6}$.

The shape of the mean spectrum can be due to a curved background between the two different chopper positions. However, especially in SS and at the shortest wavelengths of SL, the background is already very low and a curvature of a few mJy over 1.5 arcmin (distance between the two off-positions) is not likely. A discrete source in one of the background beams is also not very likely because spectra were taken at 3 different revolutions with different background positions due to the rotation of the spacecraft.

We therefore attribute the shape of the mean spectrum to an instrumental effect. Note that a similar trend is observed by Acosta [1] who finds that the ratio measured over predicted flux increases at the longest SL wavelengths for the faintest calibration star in his sample (HD 184400). What causes this chopper offset is not clear, a possible reason could be wavelength dependent vignetting.

4.5 Is the noise in adjacent channels correlated?

If the noise of adjacent channels in a PHT-S spectrum is correlated then the spectrum would contain random features that span several consecutive channels. These features could be mistaken for real.

The channel to channel correlations have been investigated by analyzing the correlation coefficients (ρ) of the distributions formed by the variables $\sigma_{target}(n)$ versus$\sigma_{target}(n+m)$, where n is a given channel number, and $m = 1, \ldots, 5$. This analysis was performed on the residual noise spectra as described in Section 4.3. The correlation coefficients were obtained for the full SS and SL arrays (64 channels) and for the last 32 channels of SS and SL. To test the validity of the method we have smoothed one residual noise spectrum according to Eqn. 3 and determined the correlation coefficients.

Table 2: *The first 4 columns give the average correlation coefficients $\rho(m)$ obtained from the residual noise spectra. The last two columns were obtained from one noise spectrum after smoothing this spectrum according to Eqn. 3.*

m	SS(1–64)	SL(1–64)	SS(33–64)	SL(33-64)	SS(33–64)	SL(33-64)
1	-0.104	-0.055	0.025	0.012	0.495	0.727
2	-0.062	-0.033	-0.030	-0.054	-0.215	0.300
3	-0.058	-0.133	0.091	0.086	-0.135	0.087
4	0.035	0.029	-0.079	-0.095	0.222	-0.083
5	0.025	0.090	-0.037	-0.037	0.260	-0.186

The correlation coefficients averaged over the 6 noise spectra are listed in Table 2. For a distribution with an infinite number of degrees of freedom, a 90% significance that the distribution is correlated requires $|\rho(m)| > 0.129$. For the unsmoothed noise spectra this criterion is just met for $\rho(3, SL(1-64))$, but the value is still below the 95% significance ($|\rho(m)| > 0.165$). For the smoothed spectrum, the first adjacent channel is highly correlated, with either an anti-correlation in the case of SS or correlation in the case of SL for $m = 2$. In the case of SS with $m = 4$ and $m = 5$ the channels are correlated again ($|\rho(m)| > 0.233$ for 99.0% significance).

We conclude that the noise in adjacent PHT-S channels do not show any correlation, therefore the noise estimates for each channel are independent.

4.6 Analysis background spectra

We have processed all observations assuming that the source and background plateaux are identical and therefore that each measurement is similar to a staring observation. For the determination of the fluxdensities it is assumed that the OLP9 dynamic calibration is valid also for the long staring measurements of 4096 s. The OLP9 error calculation as implemented in PIA has been adopted.

First inspection of the 6 spectra shows that the two spectra taken during the same revolution appear very similar whereas the spectra of different revolutions differ significantly. Some variation of the zodiacal emission is expected because of the variation of the solar aspect angle, see Table 3. Consequently, we have averaged the spectra taken on the same revolution. The resulting spectra are displayed in Figure 6. For each averaged spectrum j an uncertainty $\sigma_{repeat}(j)$ is derived for each channel i according to:

$$\sigma_{repeat}(i) = \frac{|F_\nu^a(i) - F_\nu^b(i)|}{2}, \qquad (4)$$

Table 3: *varying observing parameters for the different measurements: solar aspect angles (SAE) and roll angles during the observations.*

TDT	S.A.E.	Roll Angle
13401410	79.9	86.87
13401509	79.9	86.85
13900206	83.9	84.75
13900307	83.9	84.73
14502008	89.4	81.90
14502105	89.4	81.87

where $F^a_\nu(i)$ and $F^b_\nu(i)$ are the two fluxes of channel i. Similar to Figure 1 we have included in Figure 6 the comparison between the expected rms based on the PIA uncertainties obtained for each of the 6 measurements (σ_{PIA}) and the scatter between the three mean spectra σ_{repeat}:

$$\sigma_{repeat} = \sqrt{\frac{\sum_{i=1}^{3} \sigma^2_{repeat}(i)}{3}}, \tag{5}$$

$$\sigma_{PIA} = \sqrt{\frac{\sum_{k=1}^{6} \sigma^2_{PIA}(k)}{12}}. \tag{6}$$

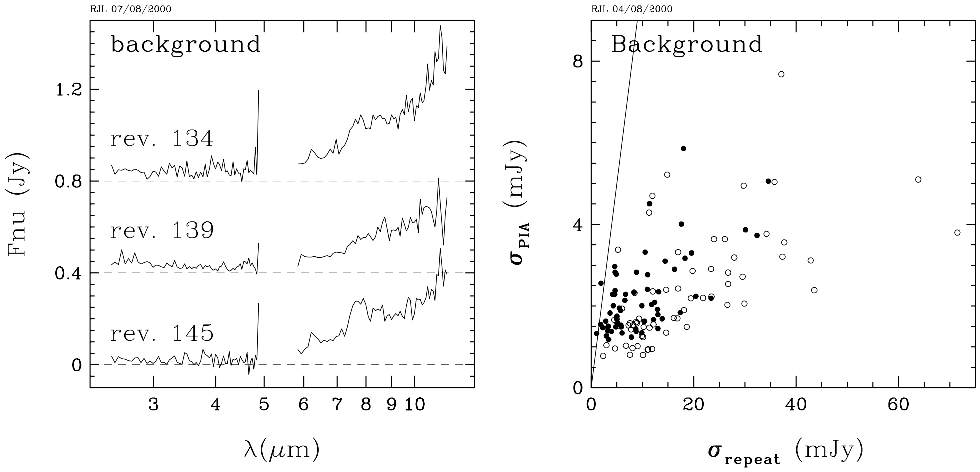

Figure 6: **Left panel:** *Composite of the PHT-S sky observations taken on different revolutions. Each spectrum is the average of 2 4096 s spectra. A constant of 400 and 800 mJy is added to the individual spectra for better comparison.* **Right panel:** *The average rms per channel from PIA as a function of the rms derived from the 6 observations. Open symbols refer to PHT-SL channels, filled symbols to PHT-SS; the line is the identity.*

The SL portion of the three spectra presented in Figure 6 appears remarkably different despite the fact that the roll angle and solar aspect angles vary mildly. In particular, the spectrum of revolution 139 exhibits a lack of PAH features at 6.2, 7.7 and 8.6 μm otherwise prominently detected in the other revolutions. It is not clear what is causing these variations. A point source in one of the chopper beams must have been noticed in the chopped observations in Figure 1. High resolution structures in the diffuse ISM could be an explanation, but the change in position of the off-positions from one revolution to the other is marginal.

Figure 6 shows that the values of σ_{PIA} are very optimistic in comparison to σ_{repeat}, in fact σ_{repeat} can be more than a factor 5 worse than σ_{PIA}. It should be noted that the long staring measurements are sensitive to errors in the dark signal subtraction and strong glitches which tend to alter the absolute signal level of a pixel. In addition, it is unknown what the influence of the chopper modulation is on the (staring) noise characteristics of the PHT-S subsystem. In any case it is clear that very faint point sources are more accurately measured in chopped mode.

The repeatability of the PHT-S photometry on brighter sources in staring mode has been investigated in more detail by Schulz [3].

5 Conclusions and recommendations

Analysis of very deep chopped observations shows that:

- the noise as derived by PIA gives a fair representation of the uncertainty per channel, although for the noisier channels (channels 33–64 of SS and SL) the noise by PIA is somewhat underestimated by about 40%;
- the channel-to-channel noise is uncorrelated;
- the noise for most channels scales with integration time according to $t^{-0.5}$, but for the noisier channels the scaling goes with a power law slightly larger than -0.5.

Since the longest measurement time available for PHT-S chopped observations is 4096 s, one can obtain an independent estimate of the chopped noise per channel for $t_{meas} > 512$ s using the noise figures derived in this report (see Tables 4 and 5). The noise figures will give a good estimate for the low noise channels and a realistic estimate at the high end for the noisy channels.

Deriving the background sky by assuming that the deep chopped observations can be treated as long staring observations shows that the noise between repeated observations is much (a factor 5) larger than the uncertainties predicted by PIA. It is not clear whether this finding holds for genuine staring observations.

It is noticed that the data were processed without visual inspection of the signals at PIA-SRD level. Manual deglitching of outliers or rejecting signal intervals affected by a prominent cosmic ray hit usually lowers the largest signal (and noise) excursions in a PHT-S spectrum. However, manual deglitching does not affect the conclusions for the chopped analysis.

Acknowledgement

B. Schulz and J. Acosta-Pulido are acknowledged for reviewing this manuscript.

References

[1] Acosta Pulido, J., "Calibration of ISOPHOT-S chopped measurements", 8 March 1999, see http://www.iso.vilspa.esa.es/users/expl_lib/PHT_top.html

[2] Acosta Pulido, J., "Calibration of ISOPHOT-S chopped measurements", 3 August 1999, draft, final version in preparation

[3] Schulz, B., "Long term responsivity stability of ISOPHOT-S", 28 May 1999, see http://www.iso.vilspa.esa.es/users/expl_lib/PHT_top.html

Table 4: *NEFD and mean spectrum for deep chopped observation on the sky, PHT-SS. The noise for a given observation is estimated from* $\sigma = \Delta F_\nu \sqrt{4096/t_{meas}}$.

Ch.	λ	ΔF_ν	F_ν	Ch.	λ	ΔF_ν	F_ν
	μm	mJy	mJy		μm	mJy	mJy
1	2.47	12.9	-7.6 ± 5.3	33	3.73	15.0	-9.7 ± 6.1
2	2.51	5.9	-16.8 ± 2.4	34	3.77	13.1	-6.4 ± 5.4
3	2.55	8.5	-6.8 ± 3.5	35	3.81	10.4	-1.4 ± 4.3
4	2.59	10.2	-14.3 ± 4.2	36	3.84	10.1	-12.7 ± 4.1
5	2.63	4.0	-12.9 ± 1.6	37	3.88	11.1	1.2 ± 4.5
6	2.67	6.4	-16.7 ± 2.6	38	3.92	13.1	-19.4 ± 5.4
7	2.71	6.1	-11.9 ± 2.5	39	3.96	21.3	-6.8 ± 8.7
8	2.75	6.3	-13.5 ± 2.6	40	4.00	10.3	-2.4 ± 4.2
9	2.79	5.2	-12.3 ± 2.1	41	4.03	13.2	5.2 ± 5.4
10	2.83	6.0	-12.6 ± 2.5	42	4.07	15.2	10.6 ± 6.2
11	2.87	7.2	-14.4 ± 2.9	43	4.11	13.0	2.2 ± 5.3
12	2.91	10.3	-16.0 ± 4.2	44	4.14	23.0	-13.1 ± 9.4
13	2.95	7.2	-10.5 ± 2.9	45	4.18	10.4	3.5 ± 4.2
14	2.99	13.2	-11.0 ± 5.4	46	4.22	21.0	1.7 ± 8.6
15	3.03	11.4	-18.1 ± 4.7	47	4.26	7.3	-0.2 ± 3.0
16	3.07	9.8	-15.0 ± 4.0	48	4.29	15.1	-16.4 ± 6.1
17	3.11	10.2	-17.2 ± 4.2	49	4.33	14.4	-6.5 ± 5.9
18	3.15	12.7	-8.3 ± 5.2	50	4.37	16.6	-3.0 ± 6.8
19	3.19	8.9	-21.4 ± 3.6	51	4.40	12.1	-5.7 ± 4.9
20	3.23	12.2	-4.8 ± 5.0	52	4.44	21.4	-2.1 ± 8.7
21	3.27	9.3	-19.4 ± 3.8	53	4.48	9.9	2.6 ± 4.1
22	3.31	9.6	-9.6 ± 3.9	54	4.51	8.8	6.1 ± 3.6
23	3.35	14.0	-14.1 ± 5.7	55	4.55	10.6	-4.5 ± 4.3
24	3.38	11.7	-25.1 ± 4.8	56	4.59	21.0	16.8 ± 8.6
25	3.42	13.1	-7.7 ± 5.3	57	4.62	10.4	2.7 ± 4.3
26	3.46	8.4	-16.2 ± 3.4	58	4.66	14.9	15.3 ± 6.1
27	3.50	6.4	-20.4 ± 2.6	59	4.69	27.8	-7.3 ± 11.4
28	3.54	13.2	-10.0 ± 5.4	60	4.73	25.7	-8.7 ± 10.5
29	3.58	11.2	-10.1 ± 4.6	61	4.76	19.9	-5.9 ± 8.1
30	3.62	8.0	-3.5 ± 3.3	62	4.80	17.8	-4.4 ± 7.3
31	3.65	10.2	-10.3 ± 4.2	63	4.84	29.6	-5.0 ± 12.1
32	3.69	21.1	-2.5 ± 8.6	64	4.87	41.6	6.7 ± 17.0

Table 5: *Same as table 4, but for PHT-SL*

Ch.	λ	ΔF_ν	F_ν	Ch.	λ	ΔF_ν	F_ν
	μm	mJy	mJy		μm	mJy	mJy
65	5.84	4.7	-2.7 ± 1.9	97	8.82	17.5	3.8 ± 7.1
66	5.93	5.3	-4.1 ± 2.2	98	8.91	14.6	0.4 ± 5.9
67	6.03	5.9	2.7 ± 2.4	99	9.00	14.9	6.5 ± 6.1
68	6.12	6.7	-5.0 ± 2.7	100	9.09	14.9	2.5 ± 6.1
69	6.22	7.0	-1.9 ± 2.9	101	9.18	12.6	-4.8 ± 5.1
70	6.31	6.5	-2.5 ± 2.6	102	9.27	20.2	1.6 ± 8.3
71	6.40	6.1	-2.3 ± 2.5	103	9.36	24.6	-4.2 ± 10.0
72	6.50	5.4	-5.4 ± 2.2	104	9.46	16.0	-2.9 ± 6.5
73	6.59	4.5	-6.3 ± 1.8	105	9.55	15.8	-0.6 ± 6.5
74	6.68	5.3	-0.9 ± 2.1	106	9.64	25.9	3.3 ± 10.6
75	6.78	8.3	-3.4 ± 3.4	107	9.73	12.1	2.2 ± 5.0
76	6.87	4.3	-2.6 ± 1.7	108	9.82	25.8	4.6 ± 10.5
77	6.97	5.5	-7.9 ± 2.2	109	9.91	18.1	-0.4 ± 7.4
78	7.06	4.7	-4.7 ± 1.9	110	10.00	12.9	1.0 ± 5.3
79	7.15	5.3	0.3 ± 2.2	111	10.09	12.8	2.4 ± 5.2
80	7.24	6.3	4.5 ± 2.6	112	10.18	19.6	-3.8 ± 8.0
81	7.34	11.4	4.1 ± 4.7	113	10.27	20.2	1.6 ± 8.3
82	7.43	11.0	-2.4 ± 4.5	114	10.36	16.4	1.3 ± 6.7
83	7.52	6.9	-3.0 ± 2.8	115	10.45	16.6	14.9 ± 6.8
84	7.62	9.2	-1.4 ± 3.8	116	10.54	15.6	8.8 ± 6.4
85	7.71	10.9	-1.9 ± 4.4	117	10.63	12.1	5.4 ± 4.9
86	7.80	7.0	-1.6 ± 2.9	118	10.72	21.5	2.7 ± 8.8
87	7.89	6.5	-1.4 ± 2.7	119	10.81	38.4	8.9 ± 15.7
88	7.99	11.6	-2.9 ± 4.7	120	10.90	32.4	-10.0 ± 13.2
89	8.08	11.9	-4.1 ± 4.9	121	10.99	17.2	8.1 ± 7.0
90	8.17	8.1	-1.3 ± 3.3	122	11.08	17.4	5.9 ± 7.1
91	8.26	13.5	1.5 ± 5.5	123	11.17	15.4	-2.7 ± 6.3
92	8.36	10.3	3.3 ± 4.2	124	11.26	18.3	20.7 ± 7.5
93	8.45	8.9	2.7 ± 3.6	125	11.35	23.3	-1.0 ± 9.5
94	8.54	8.7	-1.2 ± 3.5	126	11.44	17.9	11.4 ± 7.3
95	8.63	5.6	0.9 ± 2.3	127	11.53	26.7	9.4 ± 10.9
96	8.72	10.4	-3.3 ± 4.3	128	11.62	27.1	7.8 ± 11.0